Received: 4 October 2022 | Accepted: 21 December 2022

DOI: 10.1002/pamm.202200070

About the applicability of the theory of porous media for the modelling of non-isothermal material injection into porous structures

Jan-Sören L. Völter[1,*], **Tim Ricken**[2], and **Oliver Röhrle**[1,3]

[1] Institute for Modelling and Simulation of Biomechanical Systems, University of Stuttgart, Pfaffenwaldring 5a, 70569 Stuttgart

[2] Institute of Structural Mechanics and Dynamics of Aerospace Structures, University of Stuttgart, Pfaffenwaldring 27, 70569 Stuttgart

[3] Stuttgart Center for Simulation Science (SC SimTech), University of Stuttgart, Pfaffenwaldring 5a, 70569 Stuttgart

In this contribution we investigate the relevance of the theory of porous media for the non-isothermal modelling of material injection into porous structures. In particular, we provide a model describing the injection of cement during percutaneous vertebroplasty, which is derived by consistently following the theory of porous media. We demonstrate numerically that this model elicits unphysical behaviour under local thermal non-equilibrium conditions. No distinct unphysical behaviour is observed under local thermal equilibrium conditions. We conclude that heuristic modifications of the model equations are necessary and suspect the unphysical behaviour to be caused by contradictory modelling assumptions.

1 Introduction

Percutaneous vertebroplasty is a medical procedure in which biocompatible cement is injected into an osteoporotic vertebral body. The aim of the procedure is to stabilise the vertebral body from within by means of the injected cement undergoing curing [1]. The most common complication during vertebroplasty is the leakage of cement. This is an unfavourable outcome given, e.g., the close proximity of the spinal chord [2]. In the future, numerical simulations will be able to assist the prevention of such complications. These simulations necessitate adequate models describing the cement injection process.

Continuum models have been proposed with which micro-scale simulations yield promising results regarding the description of the injection of cement into porous structures as well as the description of the curing of the same cement after the injection [3]. The disadvantage is the computational cost associated with micro-scale simulations. This cost is far too high given the prospect of many simulations being necessary for the optimisation of operating parameters.

To avoid this inherent problem, a continuum model for macro-scale simulations has been proposed based on the theory of porous media [4]. This model assumes isothermal conditions for simplicity. This contradicts both the exothermic nature of the cement curing process and the boundary conditions of the cement injection. I.e., the injected cement typically assumes temperatures below the human body temperature at the start of the injection.

To account for this, we expand the model to the non-isothermal case, considering local thermal non-equilibrium conditions in particular. For the underlying derivation, we strictly follow the theory of porous media [5] and its applications [6, 7]. The theory of porous media is often claimed to inherently yield thermodynamically consistent models but is also regarded to be a quasi-equilibrium theory [8]. Thus, we numerically investigate the physical meaningfulness of our model for our application.

2 Model

2.1 Fundamentals of the Theory of Porous Media (TPM)

For a comprehensive overview of the fundamentals of the TPM see, e.g., the works of Ehlers [5]. The TPM describes porous media based on representative elementary volumes whose microstructure is homogenised in the sense of volumetric averaging. This allows a macroscopic description of porous media, where constituents are treated as spatially superimposed continua referred to as phases. Here, three constituents are considered, yielding a solid phase φ^S and two immiscible fluid phases φ^M and φ^C. They represent trabecular bone, bone marrow and bone cement, respectively. The local composition of the porous medium is captured by volume fractions

$$n^\alpha := \frac{\mathrm{d}v^\alpha}{\mathrm{d}v}, \quad \alpha \in \{S, M, C\}, \quad \text{with} \quad \sum_\alpha n^\alpha = 1, \tag{1}$$

defined by the ratio of the partial constituent volumes $\mathrm{d}v^\alpha$ and the aggregate volume $\mathrm{d}v$. Further, fluid saturations are defined as

$$s^\beta := \frac{n^\beta}{n^F}, \quad \beta \in \{M, C\}, \quad \text{with} \quad n^F := \sum_\beta n^\beta, \quad \text{such that} \quad \sum_\beta s^\beta = 1. \tag{2}$$

* Corresponding author: e-mail jan-soeren.voelter@imsb.uni-stuttgart.de

Denoting their local masses as $\mathrm{d}m^\alpha$ each constituent is assigned a material and an apparent density defined as

$$\rho^{\alpha\mathrm{R}} := \frac{\mathrm{d}m^\alpha}{\mathrm{d}v^\alpha} \quad \text{and} \quad \rho^\alpha := \frac{\mathrm{d}m^\alpha}{\mathrm{d}v}, \quad \text{such that} \quad \rho^\alpha = n^\alpha \rho^{\alpha\mathrm{R}}. \tag{3}$$

The description of motion of porous media borrows from the description of single-phase continua. I.e., the coordinates $\mathbf{X}_\alpha$ of the material points of constituent α evolve according to its unique motion function $\boldsymbol{\chi}_\alpha$. Therewith, the coordinates of spatial points at time t are defined as $\mathbf{x}(t) := \boldsymbol{\chi}_\alpha(\mathbf{X}_\alpha, t)$ and constituent velocities are defined as $(\mathbf{x})'_\alpha := \mathrm{d}\boldsymbol{\chi}_\alpha(\mathbf{X}_\alpha, t)/\mathrm{d}t$. In our mixed Lagrangian-Eulerian setting, solid motion is expressed via the solid displacement $\mathbf{u}_S := \mathbf{x} - \mathbf{X}_S$ and fluid motion via the seepage velocities $\mathbf{w}_\beta := \overset{\prime}{\mathbf{x}}_\beta - \overset{\prime}{\mathbf{x}}_S$.

Continuing, the aggregate and each constituent are assigned balance laws governing the conservation of mass, linear momentum, angular momentum, energy and the non-negativity of total entropy production. This set of balance laws can be simplified under certain modelling assumptions.

2.2 Non-isothermal model

In the following, we provide the preliminary assumptions underlying our model and the final set of equations which constitute our model. The derivation itself is omitted for the sake of brevity.

2.2.1 Preliminary assumptions

For our model, the mass production is neglected, the angular momentum production is neglected, the body forces are neglected ($\mathbf{b}^\alpha = \mathbf{0}$), the material densities are assumed to be constant and uniform, and quasi-static conditions are assumed. Isothermal conditions are not assumed. On the contrary, local thermal non-equilibrium is assumed.

Anticipating our simulation scenarios, the influence of solid deformations, capillary forces, as well as local thermal non-equilibrium effects on the fluid flow are negligible for our results. Therefore, for the sake of brevity, we further neglect solid deformations ($\mathbf{u}_S \equiv \mathbf{0}$), we neglect capillary pressure entirely ($p^{C\mathrm{R}} \equiv p^{M\mathrm{R}}$) and we neglect the influence of local thermal non-equilibrium effects on the fluid flow as well as on the capillary pressure ($\theta^S/\theta^\beta \approx 1$). Further, we neglect the overall momentum balance.

With these assumptions the set of governing equations reduces to two fluid volume balances and three constituent energy balances. As corresponding primary variables we choose the marrow saturation s^M, the cement pressure $p^{C\mathrm{R}}$ and the absolute constituent temperatures θ^S, θ^M and θ^C.

2.2.2 Model equations

The fluid volumes balances are given by

$$0 = (n^\beta)'_S + \operatorname{div}(n^\beta \mathbf{w}_\beta), \quad \text{provided} \quad \mathbf{u}_S \equiv \mathbf{0}, \tag{4}$$

wherein the Darcy velocities are determined by the extended Darcy filter law

$$n^\beta \mathbf{w}_\beta := -\frac{\kappa_r^\beta \mathbf{K}^S}{\mu^{\beta\mathrm{R}}} \operatorname{grad} p^{\beta\mathrm{R}}, \quad \text{provided} \quad \mathbf{b}^\alpha = \mathbf{0}, \quad \frac{\theta^S}{\theta^\beta} \approx 1 \quad \text{and} \quad p^{C\mathrm{R}} \equiv p^{M\mathrm{R}}. \tag{5}$$

Therein, $\mathbf{K}^S$ denotes the intrinsic solid permeability tensor, $\mu^{\beta\mathrm{R}}$ the dynamic viscosity and κ_r^β the relative permeability factor of constituent β. The relative permeability factors are modelled according to Brooks and Corey as

$$\kappa_r^M := (s_{\mathrm{eff}}^M)^{(2+3\lambda_{\mathrm{bc}})/\lambda_{\mathrm{bc}}} \quad \text{and} \quad \kappa_r^C := (1 - s_{\mathrm{eff}}^M)^2 \left[1 - (s_{\mathrm{eff}}^M)^{(2+\lambda_{\mathrm{bc}})/\lambda_{\mathrm{bc}}}\right], \quad \text{with} \quad s_{\mathrm{eff}}^M := \frac{s^M - s_{\mathrm{res}}^M}{1 - s_{\mathrm{res}}^M - s_{\mathrm{res}}^C}. \tag{6}$$

Therein, λ_{bc} is a uniformity parameter, s_{eff}^M denotes an effective saturation and s_{res}^β denotes residual saturations. The constituent energy balances can be written as

$$\rho^\alpha c_v^\alpha (\theta^\alpha)'_\alpha = -\operatorname{div} \mathbf{q}^\alpha + \rho^\alpha r^\alpha + \hat{\omega}^\alpha, \quad \text{with} \quad \hat{\omega}^S := \hat{\varepsilon}^S, \quad \text{provided} \quad \mathbf{u}_S \equiv \mathbf{0}, \tag{7}$$

and

$$\hat{\omega}^\beta := \hat{\varepsilon}^\beta + p^{\beta\mathrm{R}} \left[(n^\beta)'_S + \operatorname{grad} n^\beta \cdot \mathbf{w}_\beta\right], \quad \text{provided} \quad \frac{\theta^S}{\theta^\beta} \approx 1 \quad \text{and} \quad p^{C\mathrm{R}} \equiv p^{M\mathrm{R}}. \tag{8}$$

Therein, c_v^α denotes the specific heat capacity, $\mathbf{q}^\alpha$ the conductive heat flux vector and r^α an external volumetric heat supply of the constituent α. The terms $\hat{\omega}^\alpha$ are introduced for ease of notation and simply combine the direct energy production $\hat{\varepsilon}^\alpha$ with contributions of non-thermal work. The heat flux vectors are given by

$$\mathbf{q}^\alpha := -n^\alpha \kappa^\alpha \operatorname{grad} \theta^\alpha, \tag{9}$$

where κ^α denotes the thermal conductivity of constituent α. Thermal dispersion and thermal tortuosity are not considered for simplicity. The direct energy production terms of the constituents are given by

$$\hat{\varepsilon}^S = -\sum_\beta \left(\hat{\varepsilon}^\beta + \operatorname{grad}(n^\beta p^{\beta\mathrm{R}}) \cdot \mathbf{w}_\beta\right) \quad \text{and} \quad \hat{\varepsilon}^\beta := \kappa^{S\beta} a^{S\beta} (\theta^S - \theta^\beta). \tag{10}$$

Therein, $\kappa^{S\beta}$ denotes the volumetric heat transfer coefficient, specific to the interface of the solid constituent and the fluid constituent β, and $a^{S\beta}$ denotes the interface area per unit volume of the same interface. The interface between the fluid constituents is assumed to be negligible compared to the solid-fluid contact area. Under the neglect of convective heat transfer, the heat transfer coefficients are determined as

$$\kappa^{S\beta} = \frac{1}{L^F} \left(\frac{1}{\kappa^S} + \frac{1}{\kappa^\beta}\right)^{-1}, \tag{11}$$

with a given reference length L^F. The solid-fluid interface areas are approximated as

$$a^{SM} := a^{SF} \left[-0.83\,(s^C)^3 + 1.25\,(s^C)^2 - 1.10\,s^C + 0.84\right] \quad \text{and} \quad a^{SC} := a^{SF} - a^{SM}, \tag{12}$$

for $s^C \in [0.05, 0.95]$, wherein a^{SF} denotes the specific surface area of the solid constituent for a fixed porosity. Values for all of the above parameters are given in Table 1.

Table 1: Model and material parameter values.

Symbol	Value	Unit	Reference
$\rho^{S\mathrm{R}}$	1850.0	[kg/m^3]	see [9]
$\rho^{M\mathrm{R}}$	1060.0	[kg/m^3]	see [10]
$\rho^{C\mathrm{R}}$	1500.0	[kg/m^3]	cf. [3]
K^S_{ii}	5.0×10^{-8}	[m^2]	cf. [3]
λ_{bc}	3.0	[-]	arbitrary
s^M_{res}	0.05	[-]	arbitrary
s^C_{res}	0.05	[-]	arbitrary
$\mu_{M\mathrm{R}}$	1000.0	[Pa s]	arbitrary
$\mu_{C\mathrm{R}}$	1000.0	[Pa s]	arbitrary

Symbol	Value	Unit	Reference
c^S_v	2274.0	[J/(kg K)]	see [11]
c^M_v	2666.0	[J/(kg K)]	see [11]
c^C_v	1470.0	[J/(kg K)]	cf. [3]
κ^S	0.42	[W/(m K)]	see [12]
κ^M	0.42	[W/(m K)]	cf. [12]
κ^C	0.25	[W/(m K)]	cf. [3]
r^α	0.0	[W/kg]	arbitrary
L^F	1.0×10^{-3}	[m]	cf. [9, 13]
a^{SF}	2216.9	[1/m]	cf. [14]

2.3 Numerical treatment

Our model is prepared for numerical discretisation in the following. Without further explanations, the spatial discretisation is based on the Petrov-Galerkin finite element method. In particular, the Box approach is employed (e.g. [15]), allowing the employment of upwinding to prevent oscillations. The temporal discretisation is done employing a Crank-Nicholson scheme. The system of governing equations is solved monolithically using the coupled finite element solver PANDAS[1].

2.3.1 Weak formulation

Denoting the not yet specified simulation domain as Ω and the test functions as $\delta\varphi$, the weak formulation of the fluid volume balances is derived as

$$0 = \int_\Omega (n^\beta)'_S \, \delta\varphi \, \mathrm{d}v - \int_\Omega n^\beta \, \mathbf{w}_\beta \cdot \operatorname{grad} \delta\varphi \, \mathrm{d}v + \int_{\Gamma_{v^\beta}} \delta\varphi \, \underbrace{n^\beta \, \mathbf{w}_\beta \cdot \mathbf{n}}_{=:\, v^\beta} \, \mathrm{d}a, \tag{13}$$

the weak formulation of the solid energy balance is derived as

$$0 = \int_\Omega \left(\rho^S c^S_v (\theta^S)'_S - \hat{\omega}^S - \rho^S r^S\right) \delta\varphi \, \mathrm{d}v + \int_\Omega n^S \kappa^S \operatorname{grad}\theta^S \cdot \operatorname{grad}\delta\varphi \, \mathrm{d}v - \int_{\Gamma_{\mathrm{q}^S_\kappa}} \delta\varphi \, \underbrace{n^S \kappa^S \operatorname{grad}\theta^S \cdot \mathbf{n}}_{=:\, \mathrm{q}^S_\kappa} \, \mathrm{d}a \tag{14}$$

[1] **P**orous media **A**daptive **N**onlinear finite-element solver based on **D**ifferential **A**lgebraic **S**ystems (http://www.get-pandas.com)

and the weak formulation of the fluid energy balances is derived as

$$
\begin{aligned}
0 = &\int_\Omega \left(\rho^\beta c_v^\beta \left(\theta^\beta\right)'_S - \hat{\omega}^\beta - \rho^\beta r^\beta + \rho^{\beta \mathrm{R}} c_v^\beta \theta^\beta \left(n^\beta\right)'_S \right) \delta\varphi \, \mathrm{d}v \\
&- \int_\Omega \rho^{\beta \mathrm{R}} c_v^\beta \theta^\beta n^\beta \mathbf{w}_\beta \cdot \operatorname{grad} \delta\varphi \, \mathrm{d}v + \int_\Omega n^\beta \kappa^\beta \operatorname{grad} \theta^\beta \cdot \operatorname{grad} \delta\varphi \, \mathrm{d}v \\
&+ \int_{\Gamma_{\mathrm{q}_v^\beta}} \delta\varphi \underbrace{\rho^{\beta \mathrm{R}} c_v^\beta \theta^\beta n^\beta \mathbf{w}_\beta \cdot \mathbf{n}}_{=: \, \mathrm{q}_v^\beta} \, \mathrm{d}a - \int_{\Gamma_{\mathrm{q}_\kappa^\beta}} \delta\varphi \underbrace{n^\beta \kappa^\beta \operatorname{grad} \theta^\beta \cdot \mathbf{n}}_{=: \, \mathrm{q}_\kappa^\beta} \, \mathrm{d}a.
\end{aligned}
\tag{15}
$$

Therein, as Neumann boundaries we identify the volume flux boundaries Γ_{v^β} and the heat flux boundaries $\Gamma_{\mathrm{q}_\kappa^\alpha}$ and $\Gamma_{\mathrm{q}_v^\beta}$ for conductive and advective heat flux, respectively.

2.3.2 Geometry and Spatial Discretisation

A simple tubular geometry with quadratic cross-section is considered, as depicted in Figure 1. Three boundaries are distinguished. Boundary Γ_A at one end of the tube, boundary Γ_B at the opposite end and boundary Γ_C the mantle of the tube.

The finite element mesh consists of 80 hexahedral elements made up of 324 nodes. Linear shape functions are considered for all primary variables. For the employed Box approach the test functions are element-wise constant.

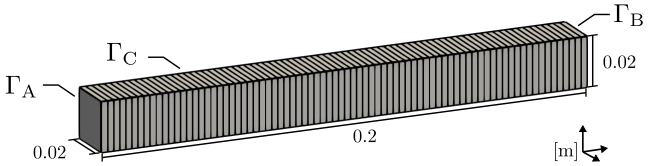

Fig. 1: Discretised simulation domain Ω with indicated boundaries Γ_A, Γ_B and Γ_C.

2.3.3 Initial and boundary conditions

For the results shown in the next section, cement is injected into the geometry at boundary Γ_A. The inflowing cement has a temperature of $308.15\,\mathrm{K}$ which is identical to the common initial temperature of all constituents. There are no external heat sources present and the entire boundary of the geometry is insulated regarding heat conduction. The initial and boundary values are given in Table 2. We choose the injection to stop after 120 seconds.

Anticipating the results, we simulate this scenario for different rates of heat transfer between the constituents. We realise this by multiplying the direct energy production of the fluids $\hat{\varepsilon}^\beta$ with a constant. This is indicated in the corresponding figures.

For the given parameter values and initial and boundary conditions all simulations are stable with a fixed time step-size of 1.0 seconds. In particular, no oscillations occur and the only notable artefacts are numerical diffusion as well as the finite nature of the spatial and temporal discretisation.

Table 2: Initial and boundary values.

Symbol	Value	Unit	Domain/Boundary
s_{0S}^M	0.95	[-]	Ω
$p_{0S}^{C\mathrm{R}}$	0.0	[Pa]	Ω
θ_{0S}^α	308.15	[K]	Ω
n_{0S}^S	0.15	[-]	Ω
s^M	0.95	[-]	Γ_B
$p^{C\mathrm{R}}$	0.0	[Pa]	Γ_B
θ^α	308.15	[K]	Γ_B

Symbol	Value	Unit	Boundary
v^M	0.0	[m/s]	$\Gamma_\mathrm{A}, \Gamma_\mathrm{C}$
v^C	5.0×10^{-4}	[m/s]	Γ_A
v^C	0.0	[m/s]	Γ_C
q_κ^α	0.0	[W/m^2]	$\Gamma_\mathrm{A}, \Gamma_\mathrm{C}$
q_v^M	0.0	[W/m^2]	$\Gamma_\mathrm{A}, \Gamma_\mathrm{C}$
q_v^C	3.40×10^5	[W/m^2]	Γ_A
q_v^C	0.0	[W/m^2]	Γ_C

3 Results

The simulation results for the considered scenario are depicted in Figures 2, 3 and 4. In all figures, the profiles of selected variables are plotted along the main axis of the geometry.

In Figure 2, profiles of the cement saturation are depicted. The cement saturation evolves corresponding to the Brooks-Corey relative permeability factors. A shock front propagates in flow direction, followed by a rarefaction fan. As ensured by

the employment of the extended Darcy filter law, the evolution of the cement saturation is not affected by temperature changes and, in particular, by the choice of the rate of heat transfer.

In Figure 3, profiles of the aggregate temperature are depicted. For these results, the rate of heat transfer is increased by factor 10^4, hence, the profiles of the constituent temperatures are identical to the profiles of the aggregate temperature and a visualisation is omitted. As is depicted, the aggregate temperature increases inside the simulation domain as time continues. Given that there are no external heat sources, this temperature increase can only be interpreted as an effect of energy dissipation, if thermodynamic consistency is to be claimed. The temperature increase does not exceed $1.0\,\mathrm{K}$ after 120 seconds of cement injection. This temperature increase is small in the context of our application. Therefore, an interpretation as an effect of energy dissipation is plausible. However, this appears to only hold with greatly increased heat transfer, i.e. under local thermal equilibrium conditions.

In Figure 4, profiles of the constituent temperatures are shown, resulting from simulations employing realistic and decreased rates of heat transfer. All profiles show results after 30 seconds.

Beginning with the cement temperature, with respect to the profiles of the cement saturation, the cement temperature peaks where the shock front of the cement saturation is located. After the peak, the cement temperature drops to a value slightly above the initial temperature and remains spatially constant. With a realistic rate of heat transfer, the cement temperature is close to the initial temperature at the inflow boundary and increases almost linearly until the peak occurs. In case of a decreased rate of heat transfer, the cement temperature first dips below the initial temperature before approaching the peak.

Continuing with the marrow temperature, with a realistic rate of heat transfer, the marrow temperature starts above the initial temperature at the inflow boundary, but drops below the initial temperature where the shock front of the cement saturation is situated. Afterwards, the marrow temperature rises slightly above the initial temperature and remains spatially constant. The lower the rate of heat transfer is chosen, the bigger the region in which the marrow temperature is below the initial temperature.

Continuing with the bone temperature, the temperature is consistently above the initial temperature. The lower the rate of heat transfer is chosen, the higher the bone temperature rises at the inflow boundary. This temperature increase is disproportional compared to the temperature changes of the cement and marrow. I.e., with the lowest considered rate of heat transfer, the marrow and cement temperature deviate from the initial temperature by $0.6\,\mathrm{K}$ at most, whereas the bone temperature deviates from the initial temperature by more than $2.0\,\mathrm{K}$ at the inflow boundary.

The described behaviour, in particular, the decrease of constituent temperatures below the initial temperature, can not be interpreted as an effect of energy dissipation. However, this means that the model as we derived it, is not inherently thermodynamically consistent.

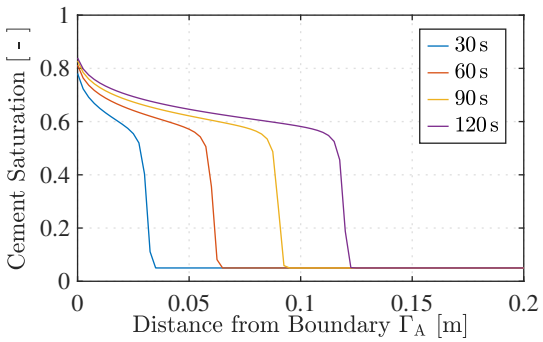

Fig. 2: Profiles of cement saturation along streamline. Profiles show results after 30, 60, 90 and 120 seconds.

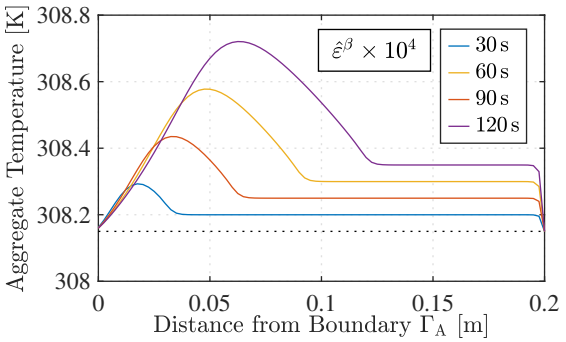

Fig. 3: Profiles of aggregate (—) and initial ($\cdots$) temperature along streamline. The rate of heat transfer is scaled by 10^4.

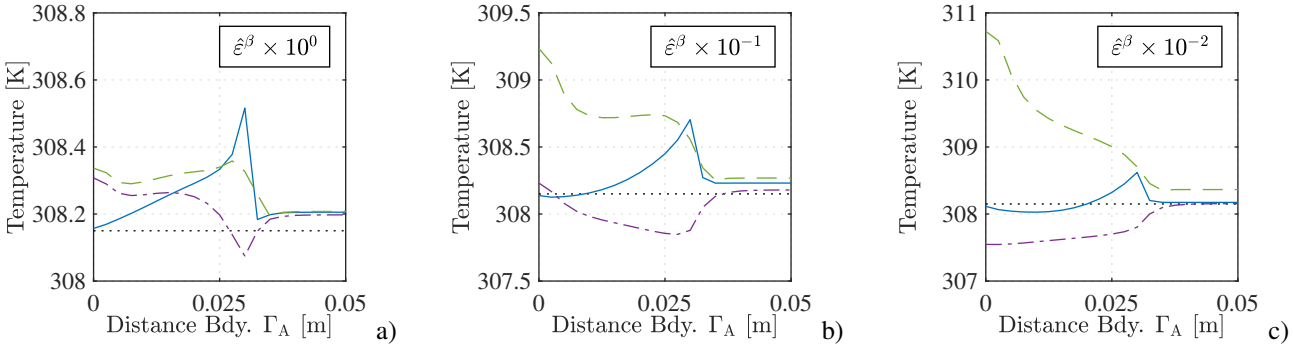

Fig. 4: Profiles of cement (—), marrow (-·-), bone (- -) and initial ($\cdots$) temperature after 30 seconds. The rate of heat transfer is scaled by (**a**) 10^0, (**b**) 10^{-1} and (**c**) 10^{-2}.

4 Conclusion

Our model does not appropriately describe the energy dissipation occurring during cement injection when considering the case of local thermal non-equilibrium. However, we derived the underlying model strictly obeying the modelling principles of the TPM. We are confident in dismissing numerical issues and algebraic mistakes as a possible source for the unphysical behaviour. Therefore, our modelling assumptions and boundary conditions must be contradictory, either towards themselves or towards the inherent assumptions of the TPM.

It is necessary to modify our model heuristically in order to avoid the unphysical behaviour we have demonstrated. Nevertheless, the model derived with the TPM is a suitable point of reference within the continuing modelling process. In future work, we will derive and present a more general model, identify the sources of unphysical behaviour and propose an adequate correction within the context of our application.

Acknowledgements We thank the Deutsche Forschungsgemeinschaft (DFG, German Research Foundation) for supporting this work by funding SFB 1313, Project Number 327154368. We further thank the DFG for supporting this work by funding - EXC2075 – 390740016 under Germany's Excellence Strategy. We acknowledge the support by the Stuttgart Center for Simulation Science (SimTech). Open access funding enabled and organized by Projekt DEAL.

References

[1] M. E. Jensen, A. J. Evans, J. M. Mathis, D. F. Kallmes, H. J. Cloft, and J. E. Dion, American Journal of Neuroradiology **18**(10), 1897–1904 (1997).
[2] E. Huntoon, Complications related to vertebroplasty and kyphoplasty, in: Seminars in Pain Medicine, (2004), pp. 233–236.
[3] S. Kolmeder, Thermomechanical-chemically coupled Material Modelling and Computational Fluid Dynamics Simulation of Adhesives in Medicine, PhD thesis, Bundeswehr University Munich, Institute for Mechanics, 2016.
[4] C. Bleiler, A. Wagner, V. Stadelmann, M. Windolf, H. Köstler, A. Boger, B. Gueorguiev, W. Ehlers, and O. Röhrle, International Journal for Numerical Methods in Biomedical Engineering **31**(11) (2014).
[5] W. Ehlers and J. Bluhm, in: Porous media. Theory, experiments and numerical applications (Springer-Verlag, Heidelberg, 2002), chap. I, pp. 3–86.
[6] W. Ehlers, International Journal of Advances in Engineering Sciences and Applied Mathematics **1**(1), 1–24 (2009).
[7] T. Graf, Multiphasic Flow Processes in Deformable Porous Media under Consideration of Fluid Phase Transitions, Report No.II-17 of the Institute of Applied Mechanics (CE), University of Stuttgart, 2008.
[8] S. Hassanizadeh and W. Gray, Advances in Water Resources **16**(1), 53–67 (1993).
[9] T. M. Keaveny, E. F. Morgan, O. C. Yeh et al., Standard handbook of biomedical engineering and design pp. 8–1 (2004).
[10] U. Gurkan and O. Akkus, Annals of Biomedical Engineering **36**(12), 1978–1991 (2008).
[11] R. McIntosh and V. Anderson, Biophysical Reviews and Letters **05**(03), 129–151 (2010).
[12] A. Feldmann, P. Wili, G. Maquer, and P. Zysset, European Cells and Materials **35**, 25–33 (2018).
[13] T. Keaveny, E. Morgan, G. Niebur, and O. Yeh, Annual Review of Biomedical Engineering **3**, 307–333 (2001).
[14] P. Coelho, P. Fernandes, H. Rodrigues, J. Cardoso, and J. Guedes, Journal of biomechanics **42**(7), 830–837 (2009).
[15] R. Huber and R. Helmig, Computational Geosciences **4**(2), 141–164 (2000).

